# On-chip active supercoupled topological cavity

*Ridong Jia, Wenhao Wang, Yi Ji Tan, Zhonglei Shen, Thomas Caiwei Tan, Zhonghua Gu, Prakash Pitchappa, Ranjan Singh**

R. Jia, W. Wang, Y. J. Tan, Z. Shen, T.C. Tan
Division of Physics and Applied Physics
School of Physical and Mathematical Sciences, Nanyang Technological University
Singapore 637371, Singapore

R. Jia, W. Wang, Y. J. Tan, Z. Shen, T.C. Tan
Centre for Disruptive Photonic Technologies, Nanyang Technological University
Singapore 639798, Singapore

Z. Gu, P. Pitchappa
Institute of Microelectronics, Agency for Science, Technology and Research
Singapore 138634, Singapore

R. Singh
Department of Electrical Engineering, University of Notre Dame
Notre Dame, IN, 46556 USA

Email: rsingh3@nd.edu

Keywords: THz on-chip cavity, THz photonic integrated circuits, supercoupled cavity, topological cavity, optothermal control

On-chip photonic resonant cavity plays a critical role in widespread applications including lasing, sensing, and spectroscopy. However, the excitation of these cavities typically relies on evanescent coupling within sub-wavelength distances, limiting flexible and precise chip integration. Here, we demonstrate an on-chip supercoupled topological cavity which is critically

coupled at 2.3-wavelength distance from a bus waveguide and remains excited even at 3.2 wavelengths, based on the supercoupling mechanism enabled by the valley vortex flow. Optothermal heating facilitates tunable quality factors and dynamic control of the supercoupling condition, allowing transitions from overcoupling to undercoupling through the critical point. Our discovery extends the waveguide-cavity excitation distance to multiple wavelengths, unlocking new possibilities for designing and controlling on-chip resonant devices, including supercoupled lasers, sensors, and modulators.

## 1. Introduction

Photonic cavity is one of the core components in photonic systems for diverse functions such as light-matter interaction[1–3], spectroscopy[4,5], and quantum optics[6]. Particularly, the chip-integrated cavities have been widely utilized in photonic integrated circuits[7–11] enabling numerous on-chip devices including surface-emitted lasers[12–16], sensors[17–22], frequency combs[23–26], and filters[27,28]. In addition to a high quality factor ($Q$ factor), which indicates a long photon lifetime and a narrower linewidth, the merit of a cavity is also characterized by the critical coupling condition[29–32] denoting the most effective excitation. The efficient transfer of photons from the excitation source to the cavity occurs when the decay rates from intrinsic loss and coupling loss are balanced. On-chip cavity excitation is typically achieved through evanescent coupling from a source waveguide. However, the excitation distance is constrained to the sub-wavelength scale due to the rapid decay of the evanescent field. Achieving evanescent critical coupling condition thereby necessitates extremely precise alignment and fabrication[33–35], posing significant challenges in designing integrated photonic cavities.

Extending excitation distance beyond sub-wavelength can potentially address the above challenges. This can be achieved through modifying waveguide mode tail length using wavelength- or sub-wavelength-scale structures such as gratings[36], metamaterials[37], and photonic crystals[38]. However, a compact and efficient long-reach coupling mechanism remained elusive until the recent discovery of photonic topological waveguide supercoupling[39]. Waveguide coupling spanning from sub-wavelength to multiple wavelengths ($\lambda$, the wavelength in free space) can be achieved with minimal coupling loss by leveraging the tunable mode tail length and momentum-conserved vortex field in valley photonic crystals (VPCs)[40–43]. Supercoupling provides a new degree of freedom (DoF) for realizing arbitrary coupling areas and ratios, enabling the optimization of chip compactness and coupling range. It unlocks the potential to create multi-wavelength supercoupled cavities, with enhanced tolerance against alignment and fabrication errors. An extended coupling area also simplifies the design of cavity-based modulators, allowing for a more flexible configuration that incorporates electro-optical[44] or acousto-optical[45] elements. Additionally, supercoupling allows for the adjustment of coupling states across multiple wavelengths, facilitating enhanced multiplexing and demultiplexing by integrating multiple cavities along the waveguide bus without strict constraints on the spacing between the waveguide and cavities.

Here, we experimentally demonstrate a supercoupled topological cavity on a terahertz silicon VPC chip. Exciting the cavity mode over a distance up to 3.2λ is achieved using a bus topological waveguide. Critical coupling condition occurs even at 2.3λ. Moreover, the topological cavity-waveguide coupled system is modified near the critical coupling condition over a distance greater than a λ, showcased by bending the robust bus topological waveguide into various shapes. Thermal control of the on-chip supercoupled topological cavity is further exhibited using an optothermal heater, demonstrating active supercoupling conditions from overcoupling to undercoupling across the critical coupling point, as well as the precisely tunable $Q$ factors. Our report extends the excitation distance of on-chip resonators, paving the way for supercoupled resonator devices including far-feed lasers, sensors, and modulators.

## 2. Results and Discussion

### 2.1 Supercoupled cavity with a multi-wavelength excitation distance

**Figure 1a** illustrates the schematics of conventional waveguide-cavity and supercoupled cavity, where the on-chip waves are fed and transition from a bus waveguide. The intrinsic loss and coupling loss of a conventional whispering-gallery cavity are indicated by $Q$ factors, $Q_i$ and $Q_c$, respectively, where $Q = \omega_0/\gamma$, $\omega_0$ is the resonant frequency and $\gamma$ is the loss rate. Critical coupling occurs at $Q_i = Q_c$ when energy is maximally coupled into the cavity, and the transmittance $T$ of the bus waveguide becomes zero as $T(\omega_0) = 0$. Evanescent coupling limits a conventional bus waveguide (bus WG) in sub-λ region of the cavity (blue region) as depicted in the left of Figure 1a. The rapid decay of evanescent field causes $Q_\mathrm{c}$ and coupling conditions extremely sensitive to the coupling distance. In contrast, the excitation of a topological cavity[31,46,47] (rectangular in right of Figure 1a) can be extended into multiple wavelengths ($m\lambda$) region (yellow region), where the supercoupling $Q$ factor $Q_{sc}$ allows for the critical supercoupling condition $Q_i = Q_{sc}$. This is attributed to the tunable mode tail lengths of the topological waveguide and the direct energy flow from the bus topological waveguide (bus TWG) along the array of unit-cell-scale vortices (red circles in Figure 1a). These vortices are the superimposition of valley momenta, excited by the topological edge state and conserved by the $C_3$ symmetric VPC bulks[39].

The coupling condition of the supercoupled cavity relies on the relation between $Q_i$ and $Q_{sc}$, which is reflected in its $T$ spectrum and the loaded $Q$ factor, $Q_l$. Non-zero transmittance at $\omega_0$ occurs in both the undercoupling ($Q_i < Q_{sc}$) and overcoupling ($Q_i > Q_{sc}$) regimes, as illustrated in

Figure 1b, where $T(\omega_0) = 0$ at critical coupling condition ($Q_i = Q_{sc}$). The $Q_l$ value varies according to the coupling conditions, as indicated by the different linewidths. Analytical $Q_l$ and $T(\omega_0)$ can be obtained based on coupled-mode theory[30,48] (detailed in Section S1, Supporting Information) as:

$$Q_l^{-1} = Q_{sc}^{-1} + Q_i^{-1} \tag{1}$$

$$T(\omega_0) = \left(\frac{Q_{sc}-Q_i}{Q_{sc}+Q_i}\right)^2 \tag{2}$$

which are plotted in Figure 1c as a function of $Q_{sc}/Q_i$ (where $Q_i$ is fixed to 1 as an example). As $Q_{sc}/Q_i$ increases (black arrow), for instance, when $Q_{sc}$ increases due to a widening gap between bus TWG and cavity, the system transitions from overcoupling (red region) to critical coupling (dash line), and ultimately to undercoupling (blue region) conditions. A zero $T(\omega_0)$ is achieved at the critical point (blue curve), and $Q_l$ (normalized from 0 to 1) decreases from its maximum (red curve). This trend is also observed in our active control experiment.

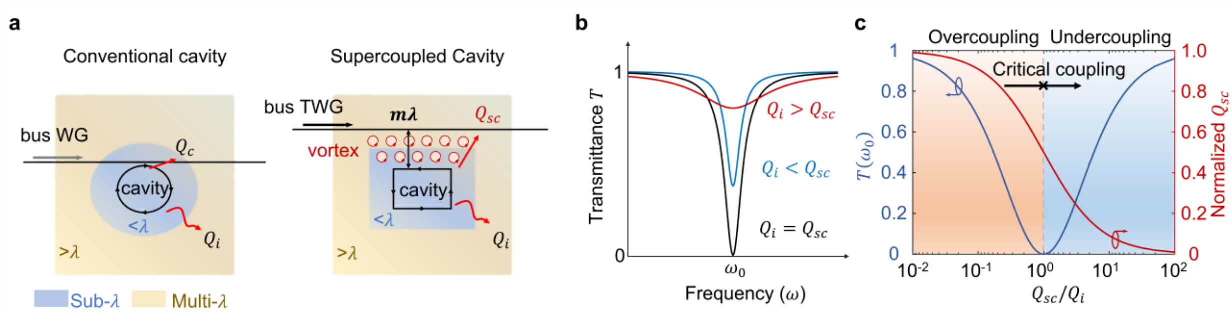


**Figure 1.** Valley-Hall photonic supercoupling in waveguide-cavity system and its coupling conditions. a) Left: schematic of conventional waveguide-cavity coupled system. The bus waveguide is limited in sub-λ region (blue region). $Q_c$ and $Q_i$ indicate coupling and intrinsic quality factors, respectively. Right: schematic of supercoupled cavity where bus TWG reaches multi-λ ($m\lambda$) region (yellow region). Red circles indicate valley vortices in coupling region, allowing for efficient energy transfer with supercoupling factor denoted by $Q_{sc}$. b) Resonance spectra with varying relations between $Q_i$ and $Q_{sc}$. $T(\omega_0)$ indicates the transmittance depths, equaling 0 for critical coupling $Q_i = Q_{sc}$ (black). c) Numerical $T(\omega_0)$ and normalized loaded $Q_l$ versus $Q_{sc}/Q_i$. An increasing $Q_{sc}/Q_i$ (black arrow) indicates the system transitioning from overcoupling ($Q_i > Q_{sc}$) to undercoupling regimes ($Q_i < Q_{sc}$), crossing the critical coupling point ($Q_i = Q_{sc}$).

The transverse-electric valley vortex in our studied cavity is illustrated by the simulated eigen modes of hexagonal unit cells in **Figure 2a**. The honeycomb lattice period is $a$ = 242.5 μm with operating wavelength of λ = 909.1 μm (0.33 THz). The spatial $C_6$ symmetry is broken into $C_3$ by altering the on-site equilateral triangular holes as $l_1 \neq l_2$, where $l_1$ = 157.6 μm (0.65$a$) and $l_2$ = 84.9 μm (0.35$a$) are the side lengths. The clockwise and counterclockwise vortices (red circles) are presented by the circular in-plane Poynting vectors (black arrows) at $K$ valley for unit cells with $\delta > 0$ and $\delta < 0$ ($\delta = l_1 - l_2$), respectively. The phase singularities at unit cell centers are observable through the simulated $\angle H_z$ (colormap). Combining bulks possessing reversed valley vortices forms topological edge states at the interfaces, which reclose the topological bandgap (right of Figure 2a). Type I and type II zigzag interfaces are formed exhibiting opposite group velocities $v_g^+$ (blue) and $v_g^-$ (black), respectively. The lengths of these topological edge mode tails are determined by the value of δ and the corresponding bandwidth[49]. A tunable range from 0.23λ to 2.7λ is demonstrated for sub-λ to $m$λ waveguide supercoupling[39]. Here, we use δ = 0.3$a$ with a mode tail length of 0.9λ, while longer mode tails are also achievable for more distant cavity excitation.

A parallelogram topological cavity is constructed using both the type I and II interfaces as shown in the left top inset of Figure 2b. The robust topological edge states ensure constructive interference in nearly arbitrary cavity shapes[50,51] when the round-trip accumulated phase is $2n\pi$ ($n$ is integral harmonic order)[52]. The simulated power flow in the supercoupling region is illustrated in Figure 2b (dash box) characterized by coupling distance $d$ and length $w$. The bus TWG mode with $K$ valley momentum and positive group velocity $v_g^+$ (blue semi-circles) excites the counterclockwise valley vortex of each unit cell as indicated by the simulated $\vec{S}$ (red arrows). These $K$-valley-conserved vortices form supercoupling loops (indicated by the blue arrow) as the flow-in energy channel to the topological cavity, leading to $v_g^-$ in the top arm of the cavity (black semi-circles) and counterclockwise cavity mode. The arrayed vortices also serve as the cavity loss channel (indicated by the red arrow) back to the bus TWG with quality factor of $Q_{sc}$. Fourier transform of $H_z$ in the coupling area (top right of Figure 2b) exhibits localizations at three $K$ points, highlighting the valley-conserved excitation of the cavity. These valley vortices in the coupling region along with the tunable mode extension of topological edge mode therefore facilitate efficient energy transfer over a $m\lambda$ distance.

We fabricated supercoupled cavities on silicon chip (see Methods) to demonstrate the $m\lambda$ excitation distance. Figure 2c plots the experimental terahertz power transmittance $S_{21}$ of the bus TWG, where the sample image is shown in the inset. A straight TWG is applied resulting in a nearly critical coupling condition of the topological cavity, when $d = 2.3\lambda$ and $T(\omega_0) = -18$ dB (red curve). Moreover, the cavity remains excited when $d$ reaches $3.2\lambda$ with $T(\omega_0)$ value of -3.6 dB (blue curve). The simulation results versus varying $d$ are illustrated in Section S2 (Supporting Information) and the temporal evolution of the supercoupled cavity excitation is displayed in Supplemental Movie 1. We further optimize the coupling region to reach critical coupling condition. A coupling distance of $1.8\lambda$ with coupling length of $4.3\lambda$ is formed through bending bus TWG into a reversed Ω-like shape, as illustrated by the sample image in Figure 2d. Experimental $T$ (red) is plotted for 4 cavity modes, where their phase spectra $\angle S_{21}$ (blue) exhibits positive gradients indicating undercoupling conditions[53]. Mode 2 approximately reaches critical coupling illustrated by the undefined phase gradient and $T(\omega_0)$ of <-40 dB. The respective $Q_l$ are 2404, 940, 328, and 6579 (fitting is discussed in Methods). The frequency-dependent terahertz comb stems from the dispersive coupling ratio between two TWGs (see Section S3, Supporting Information). The $m\lambda$ coupling distance possesses minimal coupling loss as indicated by the background transmittance >-1 dB when $d$ ranges from $1.8\lambda$ to $3.2\lambda$ (Figures 2c and 2d). The split resonant modes could possibly result from scattering perturbation caused by the sharp corners or chip surface roughness[54,55]. Our demonstrated multi-wavelength excitation distances represent a record compared to conventional waveguide-cavity systems (see Table S1, Supporting Information). Notably, the $3.2\lambda$ distance extreme can be further extended by increasing coupling length $w$ or tuning the symmetry-breaking strength $\delta$, while the sub-$\lambda$ supercoupling can be achieved by trimming mode tails through increasing $\delta$ values. Integrating supercoupled cavity into conventional integrated systems could also realize larger distance, multi-wavelength cavity excitation and minimize waveguide crosstalk on a single chip as discussed in Section S4 (Supporting Information). The scalability and a 10% fabrication error tolerance are also demonstrated in Section S5 (Supporting Information).

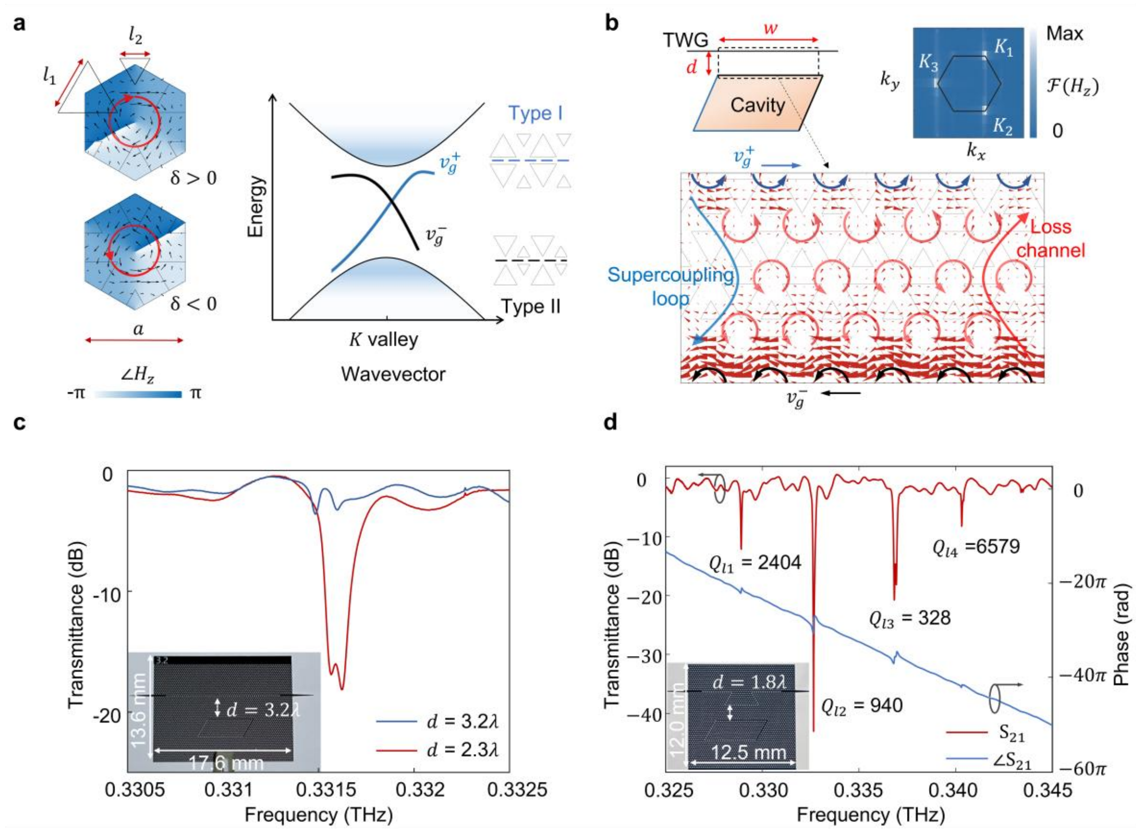


**Figure 2.** Characterization of the supercoupled topological cavity. a) Simulated valley vortices and band diagrams of topological edge states. The valley vortex is shown by the phase singularities (colormap of $\angle H_z$) and the Poynting vectors (black arrows) for unit cells with $\delta > 0$ or $\delta < 0$ ($\delta = l_1 - l_2$). Two topological edge states exhibit opposite group velocities for type I ($v_g^+$ in blue) and type II ($v_g^-$ in black) interfaces at $K$ valley. b) Simulated vortex power flow (red arrows) in the coupling region between bus TWG (blue) and the topological cavity (black). The vortex array (schematic red circles) forms excitation supercoupling loops (blue arrow) and provides cavity loss channel (red arrow). Fourier transform result is shown in the top right inset, demonstrating that the waves in the coupling region possess merely $K$ valley momenta. c) Experimental resonances of supercoupled cavity with excitation distance of 3.2λ (blue) and 2.3λ (red). d) Experimental transmittance $S_{21}$ (red) and phase $\angle S_{21}$ (blue) of the 1.8λ-coupled cavity with bent bus TWG.

## 2.2 Modifying coupling condition over *m*λ distance

The supercoupled cavity enables the modification of coupling conditions over a distance of $m\lambda$, allowing perturbations to reconfigure the vortex array of the valley Hall waveguide-cavity system. We showcase the modified coupling conditions of three samples with different bus TWG shapes at the distance of 1.4λ. **Figure 3a** presents the simulated field profiles $|H_z|^2$, with constant cavity sizes of 6.4λ × 2.5λ and fixed coupling regions of $d \times w$ = 1.4λ × 4.3λ, based on the physical lengths of the topological interfaces. Bus TWGs are configured into V-, U-, and Ω-shapes, each exhibiting various effective coupling lengths $w_{eff}$, defined as the length at which $|H_z|^2$ of the waveguide mode profile is 1/$e$ of the maximum value. The respective values of $w_{eff}$ are 4.8λ, 4.3λ, and 3.7λ, arising from the distinct valley vortex arrays at the 60° and 120° corners, as illustrated by the simulated $\vec{S}$ (red arrows) in Figure 3b for the coupling regions of Ω- and U-cavities (dash boxes), respectively. Valley vortices guide waves robustly propagating forward in bus TWG, and the on-chip waves take a shortcut through the 60° corner while mainly following the topological interface at the 120° corner, highlighted by the different power flows at the A sites (blue triangle in Figure 3b). These topology-protected bending corners result in shifts of the resonant frequency and different $Q_{sc}$, contributing to the $m\lambda$-modified supercoupling conditions. Such distant modification can also be achieved through versatile waveguide routing[56] or by tuning the mode tails[39,57–60].

The $m\lambda$ distance control of the coupling condition is experimentally validated via comparing three supercoupled cavity samples. The measured transmittances $T$ are shown in Figure 3c. We study mode 1 near 0.329 THz, where three cavities exhibit similar $T(\omega_0) < -10$ dB (top of Figure 3c) with respective resonant frequencies of 328.51 (V in blue), 328.97 (Ω in yellow), and 329.03 GHz (U in red). Their phase spectra highlight the different coupling conditions (bottom of Figure 3c): the Ω- and U-cavities (yellow and red) are over coupled, exhibiting negative phase gradients with phase changes of 2π. In contrast, V-cavity is at the undercoupling condition indicated by its less than 2π phase change and the positive gradient.

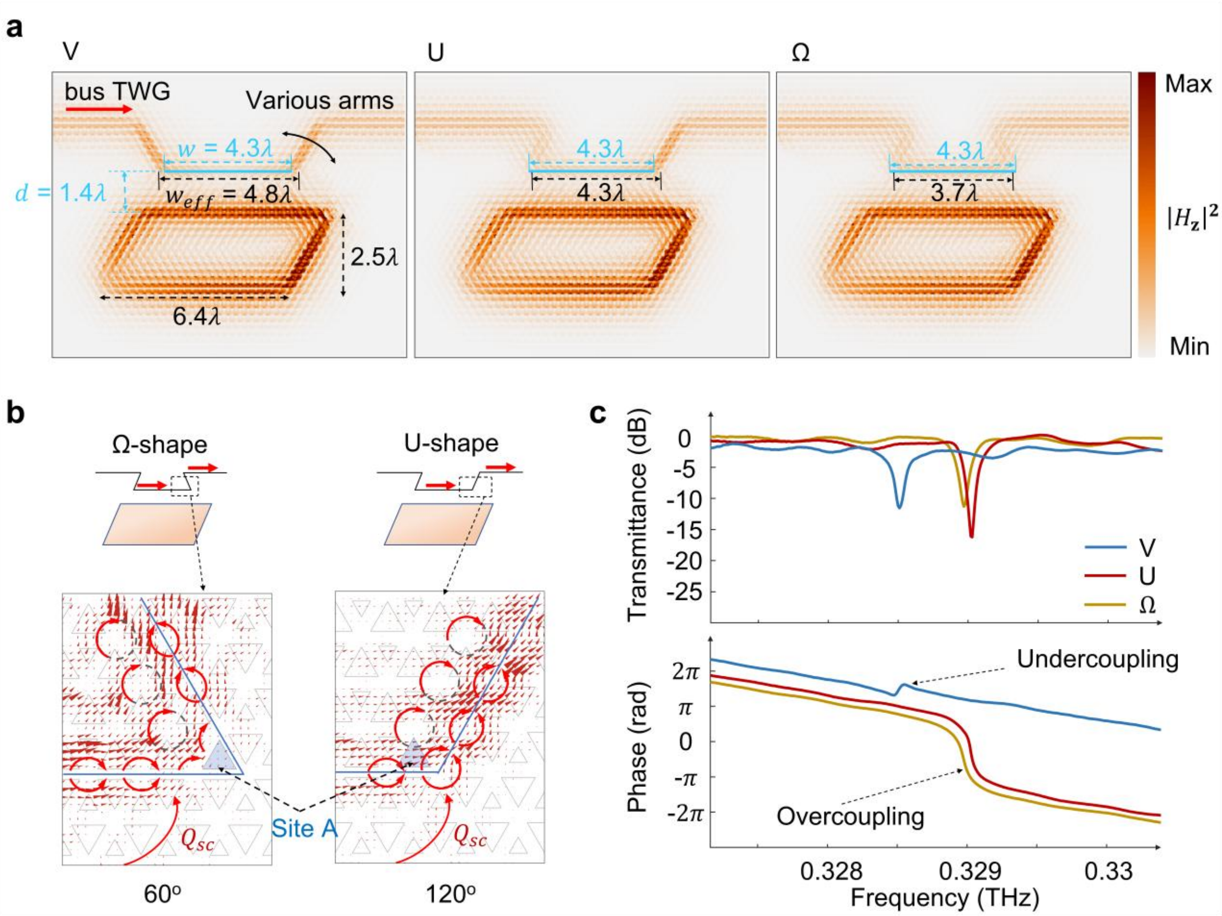


**Figure 3.** Tuning supercoupling conditions of the topological cavity by distant modifications. a) Simulated $|H_z|^2$ of three supercoupled cavity chips with identical cavity sizes and coupling regions, while excited by different shapes of bus TWGs, denoted by V-, U-, and Ω-cavities. The physical coupling regions measure $w$ = 4.3λ and $d$ = 1.4λ, with the effective coupling lengths $w_{eff}$ of 4.8λ, 4.3λ, and 3.7λ, respectively. b) Simulated Poynting vector vortices (red arrows) at the 60° and 120° corners. Blue triangles (site A) highlight their different power flows, resulting in different $Q_{sc}$ for Ω- and U-cavities. The vortex arrays are indicated by the simulated and schematic red arrows. c) Experimental transmittances and phases for V- (blue), U- (red), and Ω-cavities (yellow). Undercoupling (blue) and overcoupling (red and yellow) conditions are illustrated by the positive and negative phase gradients, respectively.

### 2.3 Active supercoupling conditions

The silicon supercoupled chips demonstrate versatile tunability, which is showcased by our thermal control experiment for active supercoupling conditions. The experimental setup is illustrated in **Figure 4a**, where a continuous wave (CW) laser as the optothermal heater targets the heating region at the corner of the chip (highlighted by the red box and the inset image) with beam diameter of 1 mm. This heating region away from the cavity region significantly exclude the effect of photo-excited carriers in silicon, which could bring phototunable cavity losses. A thermal sensor records the temperature ($\mathcal{T}$) at the center of the topological cavity, though a temperature gradient distribution occurs over the chip. $\mathcal{T}$ ranges from room temperature (25.4 °C) to a maximum of 68.2 °C when the laser input power rises from 0 to 1.24 W. The refractive index of the silicon varies due to the thermal-optical effect[61], such that the increasing $\mathcal{T}$ red-shifts (decreases) the resonant frequency $\omega_0$ and increases the loss rate $\gamma$. Both the $Q_{sc}(\mathcal{T})$ and $Q_i(\mathcal{T})$ decrease but at differentiate rates, resulting in the tuned supercoupling conditions. The measured resonance depths $T(\omega_0)$ are plotted in the $Q_{sc}$-$Q_i$ parameter space in Figure 4b, as derived from Equations. (1) and (2). Starting from overcoupling states, both the Ω- (yellow dots) and U-cavities (red dots) transition across the critical line as the temperature $\mathcal{T}$ increases. Active critical points, where $T(\omega_0) = 0$, are achieved when $Q_i = Q_{sc}$. Additionally, we verify the undercoupling condition of V-cavity, of which the results remain in the undercoupling regime (blue dots) with the absence of critical point. The maximum frequency shift is 1.4 GHz.

The measured transmittance spectra are detailed in Figure 4c versus $\mathcal{T}$ for these three cavities. The critical points are highlighted in the mid and right panels for U- and Ω-cavities with $T(\omega_0) < -30$ dB, unobservable for V-cavity in the left panel. Moreover, Ω-cavity achieves its critical coupling point at a higher critical temperature $\mathcal{T}_c = 46.4$ °C in comparison with U-cavity when $\mathcal{T}_c = 49.8$ °C. This further verifies the change of $Q_{sc}$ resulting from different bends of bus TWG (Figure 3b). These various coupling conditions are further illustrated by the phase spectra in Figure 4d versus $\mathcal{T}$. At $\mathcal{T}_c$ of U- (mid) and Ω-cavities (right), the phase gradients change from negative to positive when crossing the critical coupling conditions, while that of V-cavity (left) remains positive with less than 2π phase changes. Figure 4e elucidates the actively controlled $Q_i$ (red) and $Q_{sc}$ (blue), calculated from the measured $Q_l$ (yellow) and $T(\omega_0)$ using Equations (1) and (2). When the $Q_{sc}$ for all these three samples decrease versus the increasing $\mathcal{T}$, the $Q_i$ (red dash) and $Q_{sc}$ (blue dash) for V-cavity decrease without crossing points, indicating its undercoupling nature. In contrast, the decreased $Q_i$ crosses $Q_{sc}$ at the respective critical points for U- and Ω-cavities when $Q_l = Q_i(\mathcal{T}_c)/2$. Active supercoupling conditions for these cavities are further detailed in Section S6 (Supporting Information) for all harmonic orders, and a reference experiment with temperature control is presented in Section S7 (Supporting Information), indicating a power requirement of 28.4 mW/°C. Our thermal-control experiment provides insights into integrating versatile active controllers on these supercoupled cavity chips, such as nonlinear materials[62], MEMs[63], and high-speed modulation element[64,65].

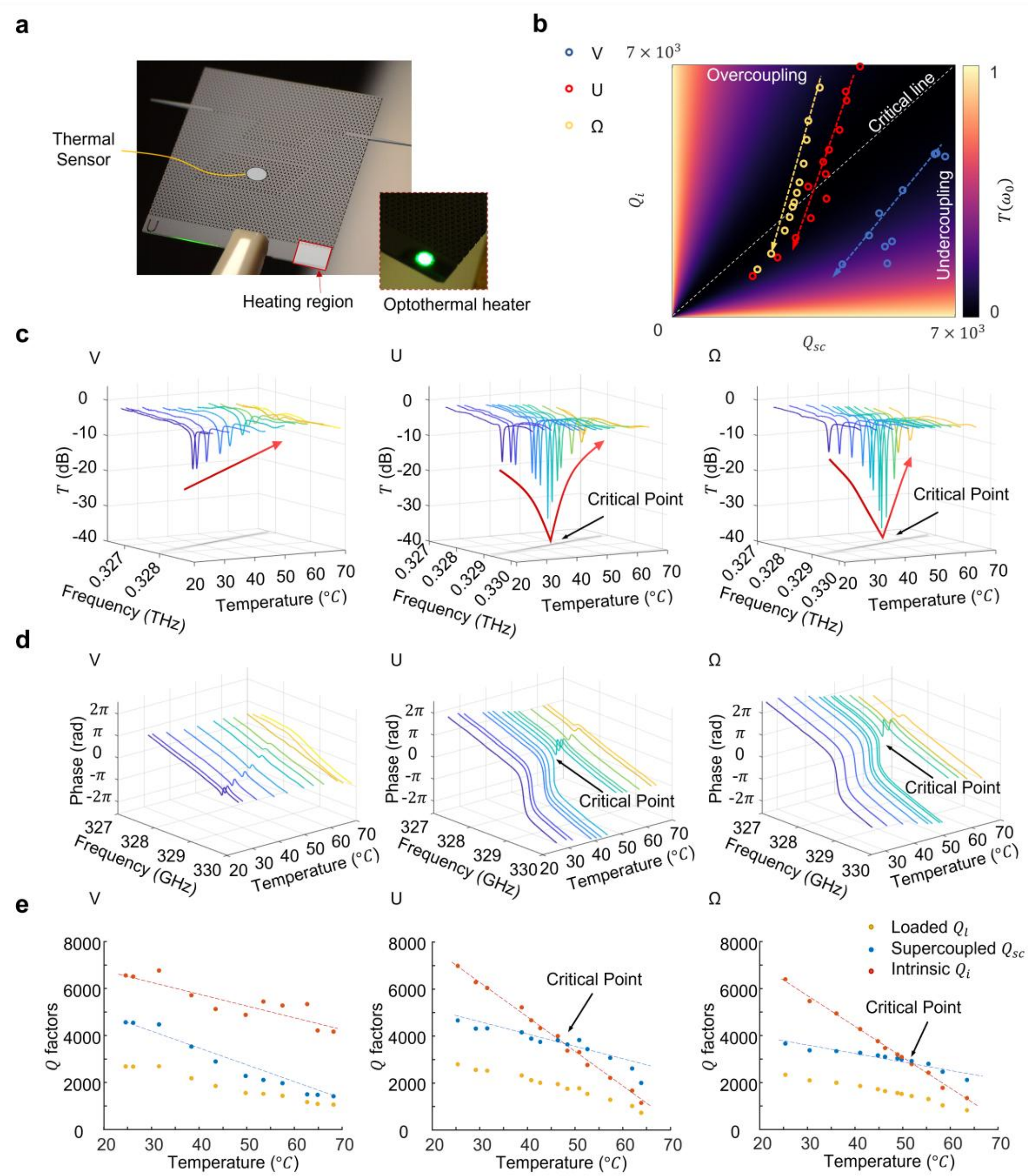

**Figure 4**. Active control of supercoupling in topological cavity. a) Image of the thermal control experiment on the supercoupled topological cavity chip. The temperature is controlled through an optothermal heater, targeting the heating region. The temperature of the cavity is recorded using a thermal sensor. b) Experimental results of V- (blue), U- (red), and Ω- (yellow) cavities, represented in the $Q_{sc}$-$Q_i$ parameter space. The positive direction of the dash arrows indicates increasing temperature $\mathcal{T}$. c, d) Experimental transmittance and phase spectrum of each cavity in (b) versus temperature $\mathcal{T}$. e) Experimental loaded $Q_l$ (yellow) and the calculated supercoupled $Q_{sc}$ (blue) and intrinsic $Q_i$ (red) for each cavity.

## 3. Conclusion

In summary, we experimentally demonstrate the supercoupled topological cavity and its active control. The valley vortex field in VPC system and the tunable waveguide mode tail substantially extend the cavity excitation distance up to 3.2λ. The critical coupling condition has been achieved when the bus waveguide is 2.3λ away from the cavity. We illustrate the precise modification of the coupling conditions near the critical points by arbitrarily bending the excitation topological waveguide at a distance beyond λ from the cavity. An optothermal method is further showcased to achieve active supercoupling conditions and precisely tunable quality factors. Supercoupled cavity with multi-wavelength excitation distance significantly addresses the short-distance alignment challenges in integrated photonics, introducing new degree of freedom for designing on-chip resonant devices, including multiplexer-demultiplexers, lasers, sensors, and modulators.

## 4. Methods

*Sample fabrication:* The fabrication of VPC supercoupled cavity was undertaken on a high-resistivity (>10 kohm·cm) 8-inch silicon wafers. 10 μm-thick photoresist was spun coated, followed by patterning the VPC design using photolithography. Deep reactive ion etching (DRIE) method was used to etch the silicon with depth over 200 μm. Back-grinding was implemented to ensure chip thickness of 200 μm.

*Experimental Setup:* The terahertz signal was generated and received using Keysight N5222B VNA, with two frequency extension modules (Z-325 and Z-500 type) operating in frequency band of 325-500 GHz. The terahertz wave was coupled into the silicon chip via a standard WR 2.2 hollow waveguide, facilitated by a taper coupler affixed to the silicon membrane. The VNA was calibrated using the standard SOLT (Short, Open, Load, and Through) waveguide calibration procedure, following which the complex S-parameters of the supercoupling chips were measured. The fiber-coupled continuous wave diode laser (STHL-525-6-105) was implemented as a heater. The heating region was positioned at the corner of the silicon chip to suppress photoexcited carriers in the topological cavity, and to create a temperature gradient to enable efficient chip cooling. The thermistor (TH10K) was applied to measure the temperature at the cavity center. Thermal-dependent spectra were recorded under equilibrium conditions, with temperature variations maintained below 0.5 °C. All resonant spectra were measured at least thrice for consistency.

*Numerical calculation:* The band diagrams of the topological edge state, the Poynting vectors of valley vortices, and the $H_z$ profile of the supercoupled cavities were obtained using COMSOL Multiphysics. The simulated chip transmittances were obtained using CST Studio Suite. The numerical *Q*-*T* plot, the *Q* factor fitting of the experimental transmittance, and the estimation of the $Q_i$ and $Q_{sc}$ were carried out in MATLAB.

The loaded quality factor was fit from the measured power S-parameter $S_{21}$ of the bus TWG. A Fano resonance function is employed to obtain the $Q_l$ and $T(\omega_0)$, expressed by the formula:

$$T = \frac{1}{1+q^2} \cdot \frac{(\epsilon + q)^2}{1+\epsilon^2}$$

where $q$ is the asymmetry factor and $\epsilon$ is the energy detuning from the resonant energy $E_0$ as:

$$\epsilon = \frac{E - E_0}{\Gamma}$$

where $E_0 = \hbar\omega_0$, $\omega_0$ is the resonant frequency, $\hbar$ is the reduced Planck constant. $\Gamma$ is the width of the resonance, based on which $Q$ factor is obtained by $Q = E_0/\Gamma$.

## Supporting Information

Supporting Information is available from the Wiley Online Library.

## Acknowledgements

The authors acknowledge the research funding supported from National Research Foundation (NRF) Singapore, Grant No: NRF-CRP23-2019-0005.

## Conflict of interests

The authors declare no competing interests.

## Author contributions

R.J. and R.S. conceived the idea. R.J. conducted the numerical analysis with the help of W.W., Y.J.T, and Z.S. The sample fabrication was performed by Z.G. and P.P. R.J. carried out the measurements with the help of T.C.T. R.J analyzed the experimental data. R.J. and R.S. wrote the manuscript with the input from all the authors. R.S. led the overall project.

## Data Availability Statement

The data that support the findings of this study are available from the corresponding author upon reasonable request.

References

[1] H. Bao, A. Cooper, M. Rowley, L. Di Lauro, J. S. Totero Gongora, S. T. Chu, B. E. Little, G.-L. Oppo, R. Morandotti, D. J. Moss, B. Wetzel, M. Peccianti, A. Pasquazi, *Nat. Photonics* **2019**, *13*, 384.
[2] Q. Zhang, Q. Shang, R. Su, T. T. H. Do, Q. Xiong, *Nano Lett.* **2021**, *21*, 1903.
[3] V. Ardizzone, F. Riminucci, S. Zanotti, A. Gianfrate, M. Efthymiou-Tsironi, D. G. Suàrez-Forero, F. Todisco, M. De Giorgi, D. Trypogeorgos, G. Gigli, K. Baldwin, L. Pfeiffer, D. Ballarini, H. S. Nguyen, D. Gerace, D. Sanvitto, *Nature* **2022**, *605*, 447.
[4] M. D. Wheeler, S. M. Newman, A. J. Orr-Ewing, M. N. R. Ashfold, *J. Chem. Soc. Faraday Trans.* **1998**, *94*, 337.
[5] A. Grinin, A. Matveev, D. C. Yost, L. Maisenbacher, V. Wirthl, R. Pohl, T. W. Hänsch, T. Udem, *Science* **2020**, *370*, 1061.
[6] F. Mivehvar, F. Piazza, T. Donner, H. Ritsch, *Adv. Phys.* **2021**, *70*, 1.
[7] A. L. Gaeta, M. Lipson, T. J. Kippenberg, *Nat. Photonics* **2019**, *13*, 158.
[8] A. W. Elshaari, W. Pernice, K. Srinivasan, O. Benson, V. Zwiller, *Nat. Photonics* **2020**, *14*, 285.
[9] J. Wang, F. Sciarrino, A. Laing, M. G. Thompson, *Nat. Photonics* **2020**, *14*, 273.
[10] S. Y. Siew, B. Li, F. Gao, H. Y. Zheng, W. Zhang, P. Guo, S. W. Xie, A. Song, B. Dong, L. W. Luo, C. Li, X. Luo, G.-Q. Lo, *J. Light. Technol.* **2021**, *39*, 4374.

[11] J. Feldmann, N. Youngblood, M. Karpov, H. Gehring, X. Li, M. Stappers, M. Le Gallo, X. Fu, A. Lukashchuk, A. S. Raja, J. Liu, C. D. Wright, A. Sebastian, T. J. Kippenberg, W. H. P. Pernice, H. Bhaskaran, *Nature* **2021**, *589*, 52.
[12] B. Peng, Ş. K. Özdemir, F. Lei, F. Monifi, M. Gianfreda, G. L. Long, S. Fan, F. Nori, C. M. Bender, L. Yang, *Nat. Phys.* **2014**, *10*, 394.
[13] K. Ishizaki, M. De Zoysa, S. Noda, *Photonics* **2019**, *6*, 96.
[14] A. Dikopoltsev, T. H. Harder, E. Lustig, O. A. Egorov, J. Beierlein, A. Wolf, Y. Lumer, M. Emmerling, C. Schneider, S. Höfling, M. Segev, S. Klembt, *Science* **2021**, *373*, 1514.
[15] C. Xiang, J. Guo, W. Jin, L. Wu, J. Peters, W. Xie, L. Chang, B. Shen, H. Wang, Q.-F. Yang, D. Kinghorn, M. Paniccia, K. J. Vahala, P. A. Morton, J. E. Bowers, *Nat. Commun.* **2021**, *12*, 6650.
[16] L. Yang, G. Li, X. Gao, L. Lu, *Nat. Photonics* **2022**, *16*, 279.
[17] S. Roh, T. Chung, B. Lee, *Sensors* **2011**, *11*, 1565.
[18] T. Yoshie, L. Tang, S.-Y. Su, *Sensors* **2011**, *11*, 1972.
[19] X. Jiang, A. J. Qavi, S. H. Huang, L. Yang, *Matter* **2020**, *3*, 371.
[20] X. Lu, S. Venkatesh, H. Saeidi, *China Commun.* **2021**, *18*, 175.
[21] A. Kumar, M. Gupta, P. Pitchappa, Y. J. Tan, N. Wang, R. Singh, *Appl. Phys. Lett.* **2022**, *121*, 011101.
[22] N. Navaratna, Y. J. Tan, A. Kumar, M. Gupta, R. Singh, *Appl. Phys. Lett.* **2023**, *123*, 033705.
[23] M. Tan, X. Xu, J. Wu, R. Morandotti, A. Mitchell, D. J. Moss, *Opt. Commun.* **2020**, *465*, 125563.
[24] S. A. Diddams, K. Vahala, T. Udem, *Science* **2020**, *369*, eaay3676.
[25] C. Bao, Z. Yuan, L. Wu, M.-G. Suh, H. Wang, Q. Lin, K. J. Vahala, *Nat. Commun.* **2021**, *12*, 6573.
[26] H. Shu, L. Chang, Y. Tao, B. Shen, W. Xie, M. Jin, A. Netherton, Z. Tao, X. Zhang, R. Chen, B. Bai, J. Qin, S. Yu, X. Wang, J. E. Bowers, *Nature* **2022**, *605*, 457.
[27] B. Min, E. Ostby, V. Sorger, E. Ulin-Avila, L. Yang, X. Zhang, K. Vahala, *Nature* **2009**, *457*, 455.
[28] X. Lu, A. McClung, K. Srinivasan, *Nat. Photonics* **2022**, *16*, 66.
[29] J. M. Choi, R. K. Lee, A. Yariv, *Opt. Lett.* **2001**, *26*, 1236.
[30] E. S. Hosseini, S. Yegnanarayanan, A. H. Atabaki, M. Soltani, A. Adibi, *Opt. Express* **2010**, *18*, 2127.
[31] A. Kumar, M. Gupta, P. Pitchappa, T. C. Tan, U. Chattopadhyay, G. Ducournau, N. Wang, Y. Chong, R. Singh, *Adv. Mater.* **2022**, *34*, 2202370.
[32] J. Hinney, S. Kim, G. J. K. Flatt, I. Datta, A. Alù, M. Lipson, *Nat. Commun.* **2024**, *15*, 2741.
[33] S. Xiao, M. H. Khan, H. Shen, M. Qi, *Opt. Express* **2007**, *15*, 14467.
[34] W. Bogaerts, P. De Heyn, T. Van Vaerenbergh, K. De Vos, S. Kumar Selvaraja, T. Claes, P. Dumon, P. Bienstman, D. Van Thourhout, R. Baets, *Laser Photonics Rev.* **2012**, *6*, 47.
[35] N. L. Kazanskiy, S. N. Khonina, M. A. Butt, *Micromachines* **2023**, *14*, 1080.
[36] L. Liu, Q. Deng, Z. Zhou, *Opt. Lett.* **2016**, *41*, 5126.
[37] Z. Li, M.-H. Kim, C. Wang, Z. Han, S. Shrestha, A. C. Overvig, M. Lu, A. Stein, A. M. Agarwal, M. Lončar, N. Yu, *Nat. Nanotechnol.* **2017**, *12*, 675.
[38] P. Dechwechprasit, R. T. Ako, S. Sriram, C. Fumeaux, W. Withayachumnankul, *Opt. Lett.* **2023**, *48*, 4685.
[39] R. Jia, Y. J. Tan, N. Navaratna, A. Kumar, R. Singh, *Adv. Mater.* **2025**, *37*, 2415083.
[40] T. Ma, G. Shvets, *New J. Phys.* **2016**, *18*, 025012.
[41] J.-W. Dong, X.-D. Chen, H. Zhu, Y. Wang, X. Zhang, *Nat. Mater.* **2017**, *16*, 298.
[42] R. Jia, S. Kumar, T. C. Tan, A. Kumar, Y. J. Tan, M. Gupta, P. Szriftgiser, A. Alphones, G. Ducournau, R. Singh, *Sci. Adv.* **2023**, *9*, eadi8500.
[43] W. Wang, Y. J. Tan, T. C. Tan, A. Kumar, P. Pitchappa, P. Szriftgiser, G. Ducournau, R. Singh, *Nature* **2024**, *632*, 522.
[44] Q. Xu, B. Schmidt, S. Pradhan, M. Lipson, *Nature* **2005**, *435*, 325.
[45] D. B. Sohn, G. Bahl, *APL Photonics* **2019**, *4*, 126103.
[46] Y. Zeng, U. Chattopadhyay, B. Zhu, B. Qiang, J. Li, Y. Jin, L. Li, A. G. Davies, E. H. Linfield, B. Zhang, Y. Chong, Q. J. Wang, *Nature* **2020**, *578*, 246.

[47] S.-Y. Yu, C. He, X.-C. Sun, H.-F. Wang, J.-Q. Wang, Z.-D. Zhang, B.-Y. Xie, Y. Tian, M.-H. Lu, Y.-F. Chen, *Natl. Sci. Rev.* **2021**, *8*, nwaa262.
[48] J. D. Joannopoulos, P. R. Villeneuve, S. Fan, *Solid State Commun.* **1997**, *102*, 165.
[49] Y. J. Tan, W. Wang, A. Kumar, R. Singh, *Opt. Express* **2022**, *30*, 33035.
[50] Y. Yang, Y. Yamagami, X. Yu, P. Pitchappa, J. Webber, B. Zhang, M. Fujita, T. Nagatsuma, R. Singh, *Nat. Photonics* **2020**, *14*, 446.
[51] H. Xue, Y. Yang, B. Zhang, *Adv. Photonics Res.* **2021**, *2*, 2100013.
[52] Y. Yang, Z. H. Hang, *Opt. Express* **2018**, *26*, 21235.
[53] L. Cong, P. Pitchappa, C. Lee, R. Singh, *Adv. Mater.* **2017**, *29*, 1700733.
[54] D. S. Weiss, V. Sandoghdar, J. Hare, V. Lefèvre-Seguin, J.-M. Raimond, S. Haroche, *Opt. Lett.* **1995**, *20*, 1835.
[55] Q. Li, A. A. Eftekhar, Z. Xia, A. Adibi, *Phys. Rev. A* **2013**, *88*, 033816.
[56] X. Cheng, C. Jouvaud, X. Ni, S. H. Mousavi, A. Z. Genack, A. B. Khanikaev, *Nat. Mater.* **2016**, *15*, 542.
[57] H. Wang, L. Sun, Y. He, G. Tang, S. An, Z. Wang, Y. Du, Y. Zhang, L. Yuan, X. He, J. Dong, Y. Su, *Laser Photonics Rev.* **2022**, *16*, 2100631.
[58] A. Vakulenko, S. Kiriushechkina, D. Smirnova, S. Guddala, F. Komissarenko, A. Alù, M. Allen, J. Allen, A. B. Khanikaev, *Nat. Commun.* **2023**, *14*, 4629.
[59] S. Kiriushechkina, A. Vakulenko, D. Smirnova, S. Guddala, Y. Kawaguchi, F. Komissarenko, M. Allen, J. Allen, A. B. Khanikaev, *Nat. Nanotechnol.* **2023**, *18*, 875.
[60] C. J. Flower, S. Barik, M. J. Mehrabad, N. J. Martin, S. Mittal, M. Hafezi, *ACS Photonics* **2023**, *10*, 3502.
[61] M. Gupta, A. Kumar, R. Singh, *Adv. Opt. Mater.* **2023**, *11*, 2301051.
[62] D. Grassani, S. Azzini, M. Liscidini, M. Galli, M. J. Strain, M. Sorel, J. E. Sipe, D. Bajoni, *Optica* **2015**, *2*, 88.
[63] N. Quack, A. Y. Takabayashi, H. Sattari, P. Edinger, G. Jo, S. J. Bleiker, C. Errando-Herranz, K. B. Gylfason, F. Niklaus, U. Khan, P. Verheyen, A. K. Mallik, J. S. Lee, M. Jezzini, I. Zand, P. Morrissey, C. Antony, P. O'Brien, W. Bogaerts, *Microsyst. Nanoeng.* **2023**, *9*, 1.
[64] M. Xu, M. He, H. Zhang, J. Jian, Y. Pan, X. Liu, L. Chen, X. Meng, H. Chen, Z. Li, X. Xiao, S. Yu, S. Yu, X. Cai, *Nat Commun* **2020**, 11, 3911.
[65] M. Samizadeh Nikoo, E. Matioli, *Nature* **2023**, 614, 451.

**Table of Content**

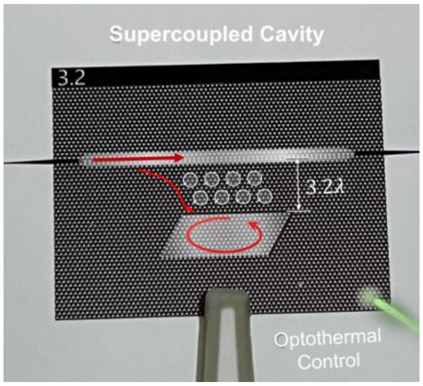


The on-chip supercoupled cavity device is demonstrated realizing a record cavity excitation distance exceeding three wavelengths, leveraging the valley-conserved supercoupling mechanism in the valley Hall topological system. This optothermal tunable design enables new degrees of freedom for supercoupled photonic cavities in mux-demux, lasers, sensors, spectrometers, and on-chip communications.